ACS Photonics

Article

Cite This: ACS Photonics XXXX, XXX, XXX−XXX

pubs.acs.org/journal/apchd5

Perfect Absorption and Phase Singularities in Plasmon Antenna Array Etalons

Annemarie Berkhout and A. Femius Koenderink*

Center for Nanophotonics, AMOLF, Science Park 104, NL-1098XG Amsterdam, The Netherlands

ABSTRACT: We present an interferometrically resolved study of the amplitude and phase response of plasmon array etalons composed of a reflective surface with a metasurface of resonant plasmonic dipole antennas in front of it. Above a minimum antenna oscillator strength (set by antenna size and density), such structures show conditions of perfect absorption. In the parameter space spanned by frequency and etalon spacing, these singular points unavoidably come in pairs and are associated with a phase singularity. The topologically oppositely charged point pairs occur around the geometric Fabry−Pérot condition. We elucidate the origin of these singularities and their continuous evolution with oscillator strength in the 2D plane spanned by optical frequency and mirror-antenna spacing. Our findings extend the understanding of Salisbury screens and of "pixels" in reflective metasurfaces for full control of amplitude and phase. Finally, our data demonstrates the limits of transfer-matrix approaches to predicting the response of arbitrary stacks of metasurfaces and dielectric layers.

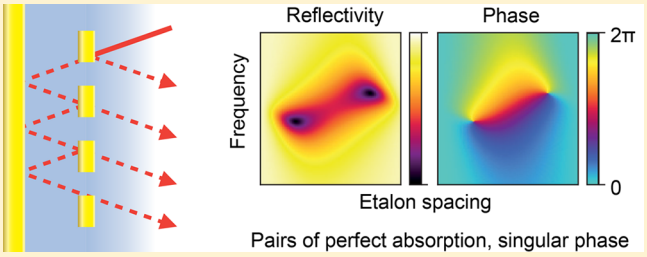

KEYWORDS: *metasurface, perfect absorption, phase singularity, pulse interferometry*

Resonant metasurfaces are of large interest in the field of subwavelength electromagnetism, from the radio frequency domain to nano-optics.[1] While most efforts to utilize metasurfaces as "flat-optics" wavefront-shapers and holograms focus on transmissive devices, "meta-mirrors" are also of interest for their tunable response in amplitude, phase, and absorption. A basic reflective geometry is that of a mirror, or ground plane, in front of which a resonantly absorbing and scattering surface is placed, typically in the form of an array of metallic or dielectric antennas with a strong scattering resonance.[2−14] Perhaps the best known example of a reflective frequency-selective surface, far predating the field of metasurfaces, is the so-called Salisbury screen in which strong absorption in a thin layer at a quarter wavelength from a mirror can be achieved, even if the layer is by itself only weakly absorbing and not resonant.[2,3] Salisbury screens with spatially patterned absorbing layers have been studied for applications ranging from RF antireflective technologies,[15] to THz and IR radiation detectors, to plasmonic sensors.[4−9] Perfect absorption in materials just in front of a reflector[10−12] has also been linked to *coherent perfect absorption*,[16,17] whereby coherent two-sided illumination of a (partial) absorber can lead to perfect absorption. More recently, reflective metasurfaces have enjoyed new interest owing to the possibility to independently control the amplitude and phase of reflected light,[14,18,19] with any phase increment upon reflection within a full 2π interval possible by tuning of the antenna resonance and antenna-mirror separation. One can distinguish three types of distinct philosophies in design: namely *etalons*, where an antenna-mirror spacing on the order of a (quarter) wavelength[9,20,21] is used; diffraction-based structures, where antennas diffractively couple into surface plasmon guided modes supported by the underlying mirror;[22] and gap-antenna based systems as pioneered by Nielsen and Pors et al.,[14,18,19] where metal nanoparticles are separated by a very narrow gap from a metal plane such that the notion of phase retardation in the gap plays no role. In the context of reflective metasurfaces, one envisions that these constructs can act as metasurface pixels that can be assembled to form a full hologram in reflection,[23] that can serve as color pixels (acting on amplitude),[24,25] that perform as polarimetric components, or that can serve as efficient reflectors with controlled phase dispersion, similar to Gires-Tournois mirrors for ultrafast pulse compression.

In this work, we present a comprehensive study of the amplitude and phase response of reflective resonant metasurface etalons in the near-infrared domain that uncovers several surprising aspects in their physics that have not been hitherto noticed. Figure 1a shows a sketch of the basic geometry of such mirror-metasurface etalons, where one reflector is a simple mirror, and the second reflector is a lattice of dipolar nanoantennas. The term "etalon" delineates that our work neither concerns gap plasmons nor diffractive coupling, and instead, it purely hinges on Fabry−Pérot etalon resonances as a function of mirror-metamirror spacing (blue curves in Figure 1b), the resonant response of the nanoantennas (shown in orange), and the hybridization of these two distinct resonance types (Figure 1c). Our amplitude and phase-resolved experiments show that from a minimum antenna oscillator threshold

Received: July 15, 2019
Published: October 16, 2019

DOI: 10.1021/acsphotonics.9b01019
ACS Photonics XXXX, XXX, XXX−XXX

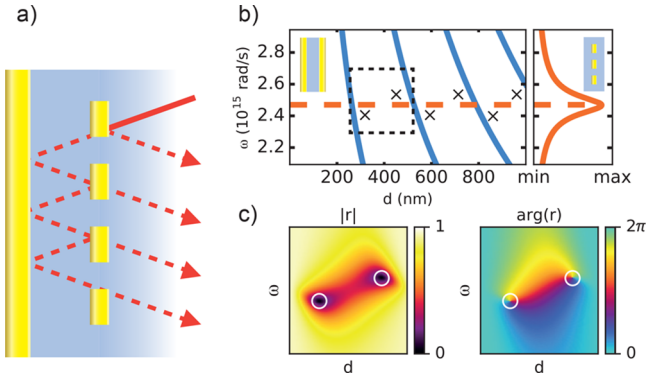

Figure 1. (a) Schematic of a plasmon array etalon consisting of a mirror and a two-dimensionally periodic, nondiffractive array of plasmonic antennas, viewed in a crosscut perpendicular to the etalon. (b) Blue: Fabry–Pérot etalon resonance as a function of mirror–mirror separation and angular frequency, relevant if the particle array were replaced by a simple mirror. Orange: the resonance of the resonant plasmonic antenna array in isolation. In the parameter plane spanned by frequency and etalon spacing, plasmon array etalons will feature pairs of points of perfect absorption and phase singularity, as indicated by crosses. (c) Response of a plasmon antenna array (square lattice, 350 nm pitch, of nanorod gold antennas resonant around $2.4 \cdot 10^{15}$ rad/s) in amplitude (left) and phase (right) for the dashed region shown in panel b. Upon hybridization of the Fabry–Pérot modes and the plasmonic resonance, a pair of singular points appears (indicated by circles).

onward, the resulting hybridization gives rise to *pairs* of conditions of zero reflection. This is not foreseen in literature reports on perfect absorption that sofar always reported, or postulated, *single* conditions of zero reflection, for instance arguing that perfect absorption is easily understood from coupled mode theory as a unique critical-coupling condition for absorptive and radiative loss of a resonator.[26,27] We show that instead in the parameter space spanned by frequency and etalon spacing, (1) the conditions of zero reflection come in pairs, and in fact must unavoidably do so because (2) they are each *necessarily* associated with a phase singularity of opposite topological charge ±1.

The main questions that our study seeks to address revolve around why such topological points of perfect absorption and phase singularity appear, and how they evolve as a function of resonator density and etalon thickness. A simple model shows that indeed from a minimum density of antennas onward, points of perfect absorption, and phase singularity inevitably appear in pairs. We examine what that entails for the phase response of metasurfaces, following the evolution of the amplitude and phase response as the density of antennas is increased. The phase singularities that we report should not be confused with optical vortices in electromagnetic fields that one can encircle as a function of spatial coordinate as studied in the field of singular optics, as they occur not in field but in a response function in parameter space. While this means that there is no fixed geometry in which the observable reflection phase becomes undefined, it does entail that the phase response swings through a full 2π for each reflectivity spectrum corresponding to any geometry with a thickness *in between* the two distinct thicknesses spanning a pair of singularities. In fact, in the context of wavepacket scattering by non-Hermitian systems, parameter-space phase singularities have been associated with a rich variety of phenomena, that include anomalous slow and fast dispersion and frequency shifts.[28,29]

With increasing antenna density the family of etalons that we study essentially evolves from a Gires–Tournois meta-etalon (particles by themselves form a weak reflector) to a Fabry–Pérot etalon (antenna layer alone is strongly reflective). Thus, our work provides a complete mapping of the fundamental trade-offs in metasurface etalons between absorption, reflection amplitude, and phase control. Finally, we also address the domain of validity of Fabry–Pérot models for such systems.

THEORY

In this study, we focus on reflective metasurfaces that can essentially be viewed as an etalon consisting of a dielectric spacer of variable thickness d, surrounded by two mirrors, the first of which is a simple gold film, and the second of which is a periodic antenna array (Figure 1a). Following refs 30,31 and the detailed overview by Alaee et al.,[9] an approximate model for such a stack is to apply the classical two-layer reflectivity model for etalons

$$r = \frac{r_a + r_m(1 + 2r_a)e^{2inkd}}{1 - r_a r_m e^{2inkd}} \tag{1}$$

where one inserts for the plasmon antenna array the reflectivity/transmission coefficients (reflectivity r_a) calculated in *absence* of the second interface. Here, $k = \omega/c$ is the wavenumber of light, n, d are the spacer index and thickness respectively, and r_m denotes the mirror reflection coefficient (which we set to −0.95, corresponding to the reflectivity of a 50 nm gold film). As distinct from the treatment of Alaee et al.[9] we have already inserted the fact that for 2D lattices of dipole scatterers $t_a = 1 + r_a$, as argued by de Abajo.[32,33] This model for etalon reflectivity r is approximate if one of the reflectors is a metasurface because it ignores diffraction orders, i.e., both real and evanescent orders that a periodic lattice of scatterers may generate. This distinguishes the physics that enters our model from that studied by[22] (diffractive coupling into surface plasmon polaritons of the mirror) and by Nielsen and Pors et al. (near-field hybridization with the mirror to form gap plasmons).[18,19]

The reflectivity of a 2D lattice of resonant scatterers in homogeneous space can be approximated using electrodynamic point dipole scattering theory, where all the near- and far-field interactions between antennas are accounted for through Ewald lattice summation.[8,30,32,34] According to de Abajo,[32] the normal incidence reflection of an antenna array reads (units used as tabulated in ref 35)

$$r_a = \frac{2\pi i k}{a^2}\frac{1}{1/\alpha - \mathcal{G}} \tag{2}$$

with α the antenna polarizability, a^2 the unit cell area, and $\mathcal{G}$ a lattice sum accounting for dipole–dipole interactions between antennas. For lattices that are sufficiently densely packed not to have propagating diffraction orders, de Abajo[32] quotes $\mathrm{Im}\,\mathcal{G} = 2\pi k/a^2 - 2/3k^3$, specific for normal incidence. The real part of $\mathcal{G}$ contains the resonance shifts of the antenna array resonance that occur due to antenna–antenna coupling, which generally depends on the lattice symmetry, particle anisotropy, and density. Because it simply renormalizes the resonance frequency but has no other consequence of relevance for our work, we absorb it into the resonance frequency ω_0 of the antenna polarizability. For a resonant antenna array, the antenna polarizability presents a Lorentzian line shape of the form

DOI: 10.1021/acsphotonics.9b01019
ACS Photonics XXXX, XXX, XXX–XXX

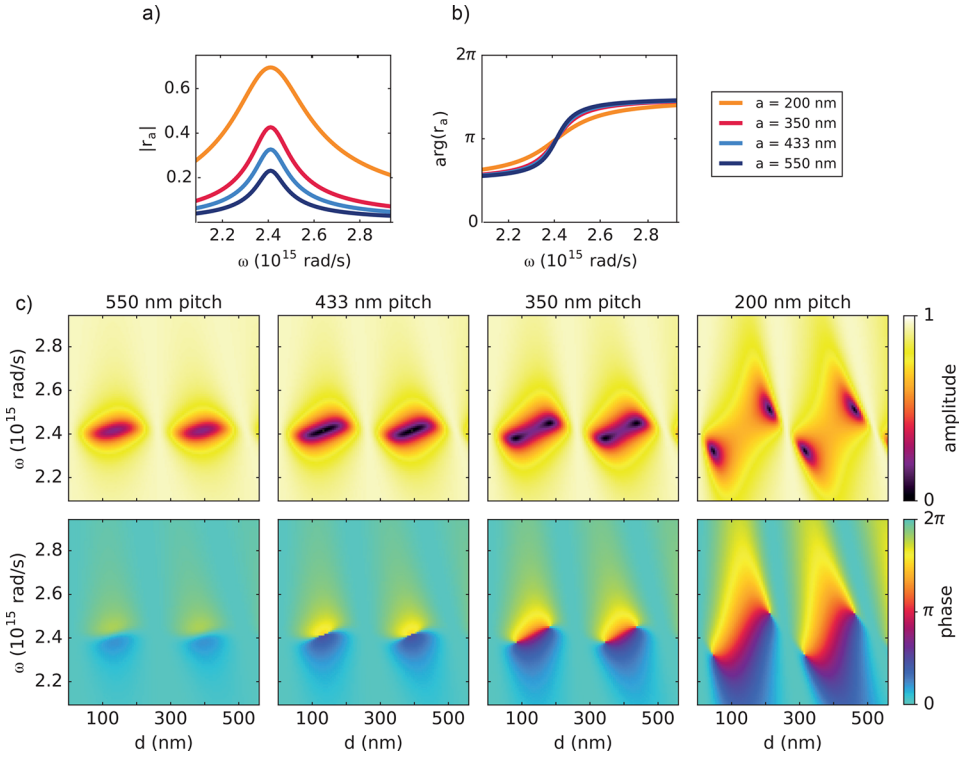

Figure 2. (a,b) Amplitude and phase of the reflectivity of a plasmon array (no backing mirror), at different antenna densities (square lattice pitch a − 550, 433, 350, and 200m as indicated above the plots), according to eqs 2 and 3). The antenna polarizability matches that of nanorod antennas made of gold studied in our experiment (Methods section), meaning that the scattering and extinction cross section per antenna matches full wave simulations. The Lorentzian response strenghtens and broadens (due to superradiant damping) with density and shows a π-phase jump through resonance. (c) Calculated amplitude (top row) and phase (bottom row) of an etalon consisting of a plasmon antenna array and a mirror, as a function of optical frequency and etalon spacing, using an antenna array pitch as in panels a,b.

$$\alpha = \frac{1}{1/\alpha_0 - i2/3k^3} \quad \text{with} \quad \alpha_0 = \frac{V\omega_0^2}{\omega_0^2 - \omega^2 - i\omega\gamma} \qquad (3)$$

where V is the effective scatterer volume, ω_0 the resonance frequency, and γ is the Ohmic damping rate. The radiation damping term[30,32] that is added to obtain the dynamic polarizability from the static polarizability[35] does not need to be evaluated in practice, owing to the fact that it is exactly canceled in the imaginary part of the lattice sum Im $\mathcal{G}$. Effectively, in a lattice radiation damping is replaced by a lattice-density dependent superradiant radiative damping, ensuring that the lattice transmission and reflection coefficients remain bounded by energy conservation for all physical choices of α_0.

Figure 2a reports the calculated reflectivity in this model for four lattices of antennas increasing in density, in absence of the back reflector. We assume that each antenna has the properties $\omega_0 = 2.4 \times 10^{15}$ rad/s, $\gamma = 9.3 \times 10^{13}$ rad/s, and $V = 6.9 \times 10^{-23}$ m^3 such that the extinction cross section on resonance equals 8.8×10^{-2} μm^2. These antenna parameters closely match a full wave simulation (COMSOL Multiphysics 5.2) of scattering and extinction cross sections of single antennas to the dipole model. The antennas are in a square lattice, with pitch a decreasing from 550, 433, 350 to 200 nm to increase density. As one would expect, the antenna-arrays show a resonant reflectivity around ω_0, with a strength that increases with density, and a π phase increment when crossing through resonance[34] (Figure 2b).

Figure 2c displays amplitude and phase of the reflectivity of the plasmon array etalon, predicted using the simple model eqs 1−3) as a function of ω and distance d between antennas and mirror, arranged according to increasing antenna density (decreasing pitch values from 550, 433, 350 to 200 nm). The pitches used for Figure 2c cycle through the canonical cases of low to very high antenna density. For the lowest density, the reflectivity barely shows a phase signature and is essentially that of the back reflector, with pockets of reduced reflection at the antenna resonance frequency only appearing for those separations where the antenna is in an antinode of the "driving field" (i.e., of the field reflected by the back reflector). Conversely, at high densities (pitch 350 and 200 nm), the reflectivity clearly shows points of zero reflection and perfect absorption, which correspond to phase singularities. These singularities come in *pairs* of topological charge ±1, meaning a full 2π phase swing when encircling them. In view of the literature, this is a surprising result. Notably, Alaee et al.[9] explicitly suggest that zero reflection instead requires the condition to be met that $r_a = -r_m$, which at constant r_m has only a *single* solution, given that r_a for our metasurface is single-valued in the complex plane. Also, this result is not covered by the commonly accepted coupled-mode theory analysis of perfect absorption by refs 26,27, which does report that at a fixed geometry perfect absorption comes with a 2π phase increment in reflectivity, but otherwise, it *a priori assumes* a single resonance and states that perfect absorption occurs at a unique matching condition for radiative and absorptive loss.

The benefit of considering the 2D plane of frequency versus etalon spacing, and to consider reflection *phase* instead of merely reflectivity amplitude of individual geometries as reported in previous works,[9] becomes apparent when

DOI: 10.1021/acsphotonics.9b01019
ACS Photonics XXXX, XXX, XXX−XXX

examining the evolution of the *pairs* of points of perfect absorption in it. Apparently, perfect absorption emerges by the creation of phase singularities in the parameter plane spanned by pitch and frequency, that topologically must come in pairs of opposite charge. As density is increased, the singularities move away from each other and from the antenna resonance frequency ω_0, toward the lines of near unity reflection. At an intermediate density of 433 nm, the reflection amplitude at minimum is low but never zero, and no phase singularities are apparent. Indeed, a numerical study suggests that this is close to a condition where the pairs of singularities of opposite charge have annihilated each other. In the remainder of this work, we first experimentally demonstrate that this behavior is real and then explain the topological origin of the singularity pairs.

RESULTS

Reflectivity Amplitude and Phase. We have built an interferometric setup (Figure 3a) to measure the amplitude and phase response of micro/nanostructures using femtosecond pulse interferometry, inspired by a design by Kop et al.[36] that we adapted to a common-path layout and that uses tunable femtosecond pulses from a Light Conversion Orpheus-F OPA. operated at 1 MHz repetition rate. As metasurface, we use gold nanorods fabricated on a flat glass substrate in square arrays of pitches 500, 433, 350, and 200 nm made by e-beam lithography (Figure 3b, Methods section). We study elongated nanorod antennas, so that by antenna length, the long-axis antenna resonance is tuned into the laser tuning range. It should be noted that since no grating diffraction orders occur, similar physics would be obtained with other (nondiffractive) lattice symmetries, with the caveat that antenna−antenna interactions in the lattice can cause shifts of the resonance frequency of the bare metasurface reflectivity r_a. Also, qualitatively the same results would be obtained with isotropic scatterers (again, correcting for the different resonance frequency), but then for both polarizations instead of just the one along the antenna axis. An SEM image of the resulting rods is shown in Figure 3b, taken before completing the etalons with a dielectric spacer and backreflector. To realize etalons, we evaporated a staircase of SiO_x giving access to thicknesses from 60 to 540 nm in 17 nm steps, on top of which we evaporated a homogeneous 50 nm gold layer as back reflector (providing an r_m of −0.95). Figure 3c shows an optical microscope image of the nanoantenna fields, viewed from the backside of the sample. Because of interference, the varying antenna−mirror spacing gives rise to a range of colors. We refer to the Methods section for an explanation of our protocol to obtain signal and reference measurements in interferometry. Incident light is polarized along the nanorods. Figure 4a shows reflection measurements for the four different pitches, sorted in order of ascending antenna density. We first examine the data set with an antenna pitch of 350 nm, which classifies as moderately strong scattering. The reflection amplitude colormap as a function of angular frequency and etalon spacing shows near unit reflection, except in pockets of spectral width 10^{14} rad/s around $\omega = 2.5 \cdot 10^{15}$ rad/s (750 nm wavelength). This wavelength and bandwidth correspond to the resonance band of the bare antenna array (the measured reflection of a bare antenna array at 200 nm pitch is 740 nm). The alternating bands of near-unit reflection at d around 270 and 520 nm and pockets of strongly reduced reflection correspond to sweeping through the Fabry−Pérot resonance and antiresonance conditions, respectively. The measured phase response reveals pairs of phase singularities for each pocket of low reflection. Tracing a loop around each of two nearby singularities results in a total accumulated phase of $+2\pi$ or -2π, indicative of opposite topological charge. Cross cuts in reflection amplitude and phase versus frequency at select thicknesses further highlight the presence of singularities (Figure 4c). On either side of a *pair* of singularities, the data (red and yellow curves) show a deep but nonetheless nonzero reflection dip with just small phase signatures. The cross cut closest to the singularity at d = 365 nm (blue) shows an overall 2π phase change over the spectrum. Right at a singularity, the reflection must vanish completely, although for practical reasons, one would not expect to be able to hit the *exact* singularity at any finite sampling of thickness and frequency. Actually measured reflectivity amplitudes closest to the phase singularities are as low as 9×10^{-3} (i.e., 10^{-4} in intensity reflectivity). Fabricating smaller increments in d would allow to measure even smaller values.

The data set at pitch 350 nm is very similar to the simple model in Figure 2c at the same pitch, highlighting the applicability of our simple etalon analysis. A remarkable deviation occurs at the smallest lattice-mirror separations, where the reflection band red-shifts significantly with vanishing separation owing to near-field coupling between atennas and mirror (further discussed below). To evidence the appearance and evolution of the singularities versus oscillator strength, Figure 4a reports data for a range of samples both more dilute

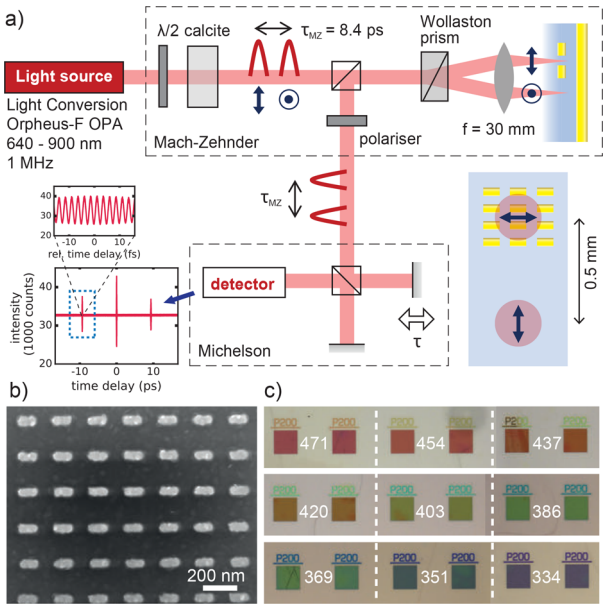

Figure 3. (a) Schematic of the setup. Femtosecond pulse pairs split temporally exit from a calcite prism into a common-path Mach−Zehnder interferometer (Wollaston prism acts as beam splitter). Reflected sample and reference are correlated by the Michelson interferometer. In the interferogram (inset left), the blue dashed region marks the left cross correlation. On the sample (inset right), each plasmon array is accompanied by an unpatterned region 500 μm downward, for the reference beam. (b) Scanning electron micrograph of a plasmon antenna array. (c) Optical micrographs of 200 nm pitch arrays, for various etalon spacings (white text, in nm). The dielectric spacer is stepped (edges marked by dashed lines), each step spanning two arrays.

DOI: 10.1021/acsphotonics.9b01019
ACS Photonics XXXX, XXX, XXX−XXX

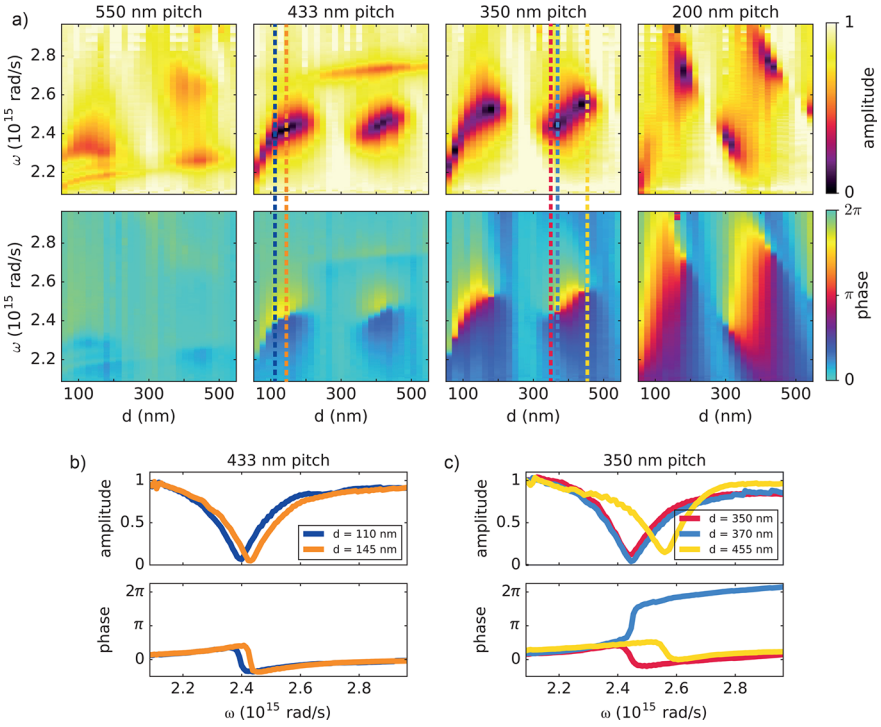

Figure 4. (a) Measured amplitude (top row) and phase (bottom row) as a function of optical frequency and etalon spacing, for plasmon antenna array etalons of pitch decreasing from 550 to 200 nm as indicated. From 350 nm onward, phase singularities and perfect absorption occur. (b,c) Crosscuts at fixed etalon spacing (as indicated by dashed vertical lines in panel a), showing reflection amplitude and phase versus frequency for 433 and 350 nm pitch.

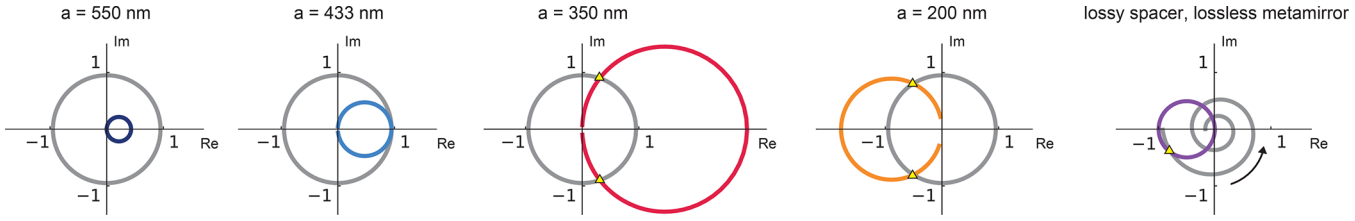

Figure 5. Graphical construction of eq 4 in the complex plane, plotting the trajectories that the left-hand and right-hand side sweep through as a function of frequency, for lattices ranging from dilute to dense, matching our experiment. In each diagram, the gray circle is $r_m e^{iknd}$ (back mirror and spacer), while the colored circles represent the trajectory of $-r_a/(1 + 2r_a)$. Intersection points (marked) correspond to the solutions of eq 4: zero reflection and phase singularities necessarily come in pairs, as soon as the array reflectivity exceeds a threshold strength (radius of the colored circles). The rightmost diagram is for a case not studied in our experiment, but common in literature:[20,26] when the spacer absorbs, the term $r_m e^{iknd}$ becomes a counterclockwise turning, shrinking, spiral. When the metasurface mirror is itself nonabsorbing, the curve $-r_a/(1 + 2r_a)$ has radius 1/2 and is centered at $-1/2 + 0i$. There is automatically one first intersection close to the metasurface resonance frequency.

and more dense than the 350 nm pitch. For the very dilute lattice, no phase singularities occur, and the reflection amplitude is only moderately modulated. Evidently the 550 nm pitch is below the threshold for phase singularity pairs and perfect absorption. For 433 nm, the sample is quite close to the threshold for appearance of phase singularities, showing the apparent "blue-yellow" discontinuity but no full 2π phase sweep, matching the calculation in Figure 2c. Measured reflectivity minima are as deep as 3×10^{-2} in intensity, but there are evidently no true zeros as there are no resolved phase singularities. Figure 4b shows cross cuts through the data at fixed spacing and as a function of frequency (dark blue and orange), which distinctly show no evidence for the 2π-phase sweep seen in the data at pitch 350 nm. On the opposite side of the threshold (i.e., pitch 350 nm and above), the reflection shows pairs of singularities of opposite topological charge, coinciding with measured $|r| < 1 \times 10^{-4}$ (for the case of 200 nm pitch). At the largest particle density, the singularities clearly move from the band of the bare antenna resonance to the hyperbolas of fixed kd-values that set the Fabry–Pérot interference condition. All these observations are consistent with the progression evident in the simple Fabry–Pérot model that we plotted in Figure 2.

Topological Origin of the Singularities. Returning to the Fabry–Pérot model, it is immediately evident that a mirror-metasurface etalon will attain exactly zero reflection, and hence perfect absorption, when the numerator of eq 1 crosses zero. This requires the condition:[33]

$$r_m e^{2inkd} = \frac{-r_a}{(1 + 2r_a)} \tag{4}$$

quite distinct from the condition $r_m = -r_a$ listed for the Fabry–Perot description of perfect absorption by Alaee et al.[9] A graphical solution for the case at hand is very insightful (Figure

DOI: 10.1021/acsphotonics.9b01019
ACS Photonics XXXX, XXX, XXX−XXX

5). For nonabsorbing spacers, the lefthand side of eq 4 circumscribes a full circle in the complex plane of radius r_m around the origin (gray dashed), each time that one sweeps the product of (optical) spacing nd and wavenumber k a full 2π (assuming nondispersive mirror reflectivity r_m). Additionally, the right-hand side of eq 4 as a function of frequency traces out a curve in the complex plane that for a Lorentzian antenna model (eq 3, same antenna properties as used in Figure 2) happens to also be a circle (colored lines). However, this circle is displaced exactly by its radius along the real axis and can have essentially any radius, increasing with the oscillator strength per unit area. As the oscillator strength is increased and the peak antenna reflectivity goes through $r_a = -1/2$, the radius goes through infinity, after which the circumscribed circle shrinks again in radius, now in the opposite part of the complex plane (negative real part).

The topology of the problem in the complex plane immediately shows a number of salient features. First, there are no solutions for a zero in etalon reflection below a minimum antenna oscillator strength (blue curves in Figure 5), as the circular locus traversed by $-r_a/(1 + 2r_a)$ is too small to cross $|r_m|$. Second, above this minimum, the equality always has a *pair* of solutions (i.e., there are two distinct values for $\exp(2inkd)$ at which reflection vanishes). Hence reflection zeroes will always come in pairs, with pairs repeating at half-integer wavelength spacing between layers. While each of the two distinct solutions actually provides a countably infinite set of replicas at larger thicknesses, one can nonetheless uniquely group the pairs into those that belong to the same multiple of 2π added to $2nk \bmod 2\pi$ by noting that as a function of antenna density, one can track how the pair splits off from a single singularity right at the critical thickness of touching circles (Figure 5b). Each pair of absolute zeroes in reflectivity are associated with a pair of phase singularities of opposite charge. This is evident from the Cauchy argument principle applied to the realization that reflectivity in eq 1 with the applied model for the metasurface reflectivity is a meromorphic function of ω an d. A fourth prediction that is evident from Figure 5 by tracing the location of the intersection points is that when the zeros just appear (oscillator strength just above threshold), they will do so close to the reflection resonance of the bare particle array (note that also at this point the condition $r_a = -r_m$ from literature does not hold). For increasing oscillator strength, the zeros shift toward $r_m e^{2inkd} = \pm i$, or equivalently toward the Fabry–Pérot resonance condition ($e^{2inkd} = 1$ for near-unit efficiency mirrors). Both the Fabry–Pérot calculations in Figure 5, and the experimental data sets in Figure 4c illustrate exactly these scenarios: going from no intersection at low density, via the point of touching at intermediate pitch of 433 nm, to the regimes of intersection at moderate and strong oscillator strength. Commensurate with the discussion of Figure 5, only the cases of intersecting circles show perfect absorption, with concomitant pairs of phase singularities. The transition from pitch 433 to 350 nm documents the birth of two oppositely charged singularities. Here it should be noted that our experiment does not visualize the very first singularity, not just because our sample does not afford access to sufficiently thin spacers, but also because physics *beyond* the Fabry–Perot model shifts the first singularity to the red of our laser range.

In the literature on perfect absorption, a very well-known viewpoint is that it can be described as critical coupling of a single-mode resonator to the far field by matching of loss and damping rates.[20,26] To connect to this viewpoint, we observe that the critical coupling formula for a single resonance with a single input/output port has as an essential property that the real-frequency zero in the scattering matrix or response function at critical coupling is associated with a nearby pole in the complex frequency plane, where the real part of the frequency is that of the perfect absorption condition. The etalon response function encoded in eqs 1–3 evaluated at thicknesses where perfect absorption occurs also carries complex-frequency plane poles at frequencies near to the zero in the scattering matrix. This highlights that the metasurface etalons realize the physics reported by Solli et al. and Asano et al.,[28,29] with the associated implications of parameter-space singularities and perfect-absorption points on anomalous dispersion properties. At the same time, it should be noted that the literature critical coupling conditions arguments[20,26] in essence *postulate* a single resonance with its resonance frequency and damping rate, without any predictive power to decide on the existence or number of these poles or their parameters on the basis of the constituents of the etalon, as opposed to the analysis in this work. Effectively, the single-mode critical-coupling model can parametrize [by fitting parameters], but not predict, the perfect absorption and phase response spectra. This parametrization is only valid close to singular points: actual reflectivity spectra (vertical cuts in our calculated diagrams) can be distinctly non-Lorentzian, meaning that the single-pole approximation of refs 20,26 does not apply. A further subtlety in this argument is that some reports on perfect absorption actually deal with *absorbing spacers* surrounded by nonabsorbing reflectors r_a (see refs 20,26). To deal with this case, one should consider that now the left-hand side of eq 4 turns from a circle into a spiral that for a near-lossless back reflector starts close to $r_m = -1$ and then turns clockwise and shrinks to the origin with increasing kd. If the metasurface reflector is itself lossless, the conditions $t_a = 1 + r_a$ together with $|t_a|^2 + |r_a|^2 = 1$ constrain its reflectivity r_a, and coincidentally also $-r_a/(1 + 2r_a)$ to a circle of radius exactly 1/2, centered at $-1/2 + 0i$ in the complex plane. In this topologically different scenario, if the metasurface has a resonance (at resonance for a nonabsorbing metasurface automatically $r_a = -1$), there is automatically a *single*, first crossing with the spiral, that is, a *single* thickness for perfect absorption occurs, at a frequency close to the resonance. This single first resonance is the case studied in ref 26 and ref 20. Just increasing thickness from this first perfect absorption condition onward, while remaining at the same frequency, will not reveal further conditions of perfect absorption unlike the case of a lossless spacer. However, in parameter space, there is a further infinite series of pairs of singularities, with frequency detuning steadily increasing with spacer thickness (within the assumption of a nondispersive refractive index).

Beyond the Fabry–Pérot Model. Finally, we turn to the differences between our experimental results and the simple Fabry–Pérot model. First, near-field coupling between the antennas and the mirror substrate causes a significant resonance redshift at small separations for each of the antennas arrays and hence also for the collective response. This is especially clear for the intermediate densities (433 and 350 nm). This effect was predicted to occur in this context by Kwadrin et al.[30] To describe the redshift, a model that includes near-field coupling to the mirror is required. One viewpoint is that in this regime, one enters the regime of gap plasmons studied by Pors et al.,[19] where it is more fruitful to solve for the

DOI: 10.1021/acsphotonics.9b01019
ACS Photonics XXXX, XXX, XXX–XXX

antenna-mirror system as a resonator, instead of applying a Fabry−Perot model. Another viewpoint is appropriate for the description of stacked (meta)surfaces as multilayers. For standard multilayers, transfer matrix/S-matrix methods are robust because the interface reflection constants apply at any spacing to adjacent layers, owing to the fact that they follow directly from boundary conditions on parallel field components of **E**, **H**. Instead, metasurfaces are only effectively homogeneizable but not actually homogeneous. At small spacings, the antennas hybridize with their own mirror image. This "backaction" effect is mediated by near-fields, that is, by evanescent lattice diffraction orders that are not contained in eqs 1 and 2, and that would only be accounted for if the layer S-matrix method that gave rise to eq 1 was expanded to a full Fourier modal method. This observation essentially impacts any effort to design multilayer stacks of metasurfaces, as is pursued, for instance, for analog processing of images[37] and metasurface polarimetry.[31] Clearly, standard transfer matrix approaches to construct the response of a stack out of the response of constituents only hold if (meta)surfaces are widely spaced (in excess of $\sim \lambda/2\pi$).

A second and distinct deviation between our data and the simple Fabry−Pérot interference model is that for larger pitches diffractive coupling can occur into grazing angle grating diffraction orders in the glass or possibly surface plasmon polariton (SPP) waveguiding modes, at least for sufficiently small wavelengths and large pitches.[32] These features require grating-assisted parallel momentum matching of incident light to the glass/SPP and would hence occur in the measured reflectivity diagrams as horizontal lines, sharply defined in frequency and not (strongly) dependent on spacer thickness. This corresponds to the scenario considered by Christ et al.[22] For diffraction into a waveguide mode, or into a grazing grating diffraction order, of a given effective index n_{eff}, diffractive coupling from normal incidence occurs at $\lambda = n_{\mathrm{eff}}a$, with a the lattice pitch. For the densest lattice, no diffraction condition can be met. However, diffractive coupling is clearly evident for pitches 433 and 550 nm, through dark, narrow, and near-horizontal features of reduced specular reflectivity near 680 nm respectively 860 nm. We observe apparent indices of around 1.57, exceeding the index of the glass substrate and cover layer. Furthermore, the diffraction features are not quite horizontal but disperse slightly with mirror-particle spacing, indicating that the relevant effective index n_{eff} varies somewhat with spacer thickness at small separations. This points to the fact that the grating incoupling is into a surface plasmon polariton mode (since the index exceeds that of the dielectric layers) that is a hybrid between the surface plasmon polariton of a flat glass-gold interface and the particles, as evidenced by the separation dependence of n_{eff}. At the largest pitch, the diffraction condition overlaps partially with the particle resonance, leading to a more complicated response. Indeed, overlapping particle and diffraction responses can give rise to intricate Fano-type lineshapes, as is well-studied in the field of surface lattice resonances and waveguide plasmon-polaritons.[38]

DISCUSSION

To summarize, we have reported the amplitude and phase response of metasurface etalons of which the backreflector is an unstructured mirror, and the other is a resonant antenna array. Our theoretical and experimental results both show that from a minimum threshold oscillator strength density, controllable via antenna density and cross section, *pairs of points* of perfect absorption necessarily appear in the parameter space spanned by frequency and mirror-antenna separation space. Furthermore, these points are necessarily associated with pairs of phase singularities of charge ± 1. As the antenna oscillator strength and density are increased, the singular points move away from the bare antena resonance, and from the condition that the antenna must be in the antinode of the backreflector standing wave, and shift toward the Fabry−Pérot conditions of a standard mirror-sandwich. The singularities in parameter space directly imply for the response of any fixed geometry that meets a condition of perfect absorption that the concomitant reflection spectrum will have a phase that is never singular but will show a full 2π phase increment. Singularities occur not only in the parameter space spanned by frequency-pitch but also in parameter spaces spanned by frequency and antenna oscillator strength—and furthermore for fixed geometries that lead to singular behavior in frequency-incidence angle space and fixed-frequency k-space. Our work has several interesting repercussions. It adds to the understanding of the general design rules for reflective metasurface "pixels" for reflection amplitude and phase control. The presence of the singular points means that reflection amplitude over a large range down to true zero is possible, and reflection phases can occur over the entirety of 0 to 2π. For the given material system, reflectivity of >50% can be maintained at any desired phase, using the densest lattices. In our work, the rod-shaped antennas imply phase control for just one linear polarization channel, meaning that these reflective metasurfaces will also allow polarimetric operations such as polarization-selective absorption and retardation. Furthermore, several authors have previously suggested that sensing schemes could benefit from working around phase singularities in parameter spaces (i.e., around points of zero reflection).[39−43] In the systems considered here, the phase singularities are dependent on one hand on the product nkd (giving sensitivity to frequency, and etalon refractive index and spacing) and to r_a on the other hand (sensitivity to antenna resonance). In the framework of pulse control, scattering-matrix zeros are associated with anomalous dispersion properties as proposed by Solli et al. and studied in microcavitiy systems in experiments[28,29] The simple metasurface etalon system provides this physics, which could be applicable to the design of ultrafast dispersive mirrors. Finally we note that the *deviations* between the simple etalon model and the data at small mirror-metasurface separation also point to interesting aspects of designing *stacked* metasurfaces, as is pursued for metasurface polarimetry, as well as for analog computing with metasurfaces,[31,37] where one would hope to concatenate functions by stacking surfaces. Transfer matrix theory will only predict the response of closely spaced stacked metasurfaces if one keeps track of evanescent diffracted orders.

METHODS

Interferometry Setup. We implemented an interferometric setup to measure the amplitude and phase response of micro/nanostructures due to the design by Kop et al.,[36] adapted to a common-path layout. The principle is that the sample is placed in one arm of a Mach−Zehnder interferometer which is fed by a femtosecond pulse train. The second arm provides a reference path with a fixed, nonzero time delay that well exceeds the pulse duration. This ensures that at the output of the interferometer, the sum $E_r(t + \tau_{MZ}) + E_s(t)$ of two temporally separated pulses emerge, one of which has traveled through the reference arm and was delayed

DOI: 10.1021/acsphotonics.9b01019
ACS Photonics XXXX, XXX, XXX−XXX

by an amount τ_{MZ}, and the other one of which has interacted with the sample. Next, this double-pulse train is fed into a scanning Michelson interferometer, to record an interferogram $I(\tau)$ as a function of time delay τ, that is

$$\int \left| (E_r(t + \tau_{MZ}) + E_s(t)) + (E_r(t + \tau_{MZ} + \tau) + E_s(t + \tau)) \right|^2 dt \quad (5)$$

As argued by Kop et al.,[36] the interferogram will show around its zero delay the sum of the field−field autocorrelations of the sample and reference pulse, while at scan delays near $\pm \tau_{MZ}$, cross-correlations of the reference and sample pulse appear. This allows to retrieve back the complex-valued sample transfer function $H(\omega)$ since

$$\mathcal{F}I_{CC}(\tau) \propto H(\omega)|E_r(\omega)|^2 e^{i\omega\tau_{MZ}} \quad (6)$$

The input pulse spectrum $|E_r(\omega)|^2$ can be retrieved either from the autocorrelation (blocking the sample arm) or from a reference measurement on a reference sample with $H(\omega) = 1$.

Figure 3a shows the realization of this principle in our work, where the difference with Kop et al.[36] is that we have built the Mach−Zehnder interferometer in an almost entirely common path layout, so that reference and sample beam both pass through the same optics, arriving at only slightly offset locations on the sample. To arrange this, we follow a design by van Dijk.[44] The femtosecond pulse train of a Light Conversion ORPHEUS-F OPA at 1 MHz is polarized at 45 deg relative to the lab frame (taking 0 degrees to be vertically polarized) and then fed through a birefringent calcite block of 15 mm length. This results in two orthogonally polarized (horizontal and vertical) pulses at a fixed temporal delay of 8.4 ps, traveling along the same optical axis. Next, these beams are split in a 1 degree angle by a Wollaston prism. Upon focusing with a lens or microscope objective, this means that two foci arise, offset in time by 8.4 ps, as well as being offset in space. In our setup, we use a simple focusing lens (f = 30 mm, achromat), resulting in a spatial separation of 500 μm. Our setup can be operated both in reflection and in transmission, by ensuring that the collection path follows an identical geometry to the excitation path. In this work, we focus on reflection, in which case we simply use the fact that after passing through the same Wollaston prism the reflected pulses are collinear again. We split off the reflected light using a beam splitter between Wollaston prism and calcite and project the orthogonally polarized reference and sample pulses on the same polarization axis using a polarization analyzer at 45 deg to the lab frame. This is the point of recombination of pulses in the Mach−Zehnder interferometer. Next, the copolarized and collinear pulse pair is fed into a Thorlabs OSA202C spectrum-analyzer, which is in fact a scanning Michelson interferometer. We read out interferograms as shown in Figure 3a inset, clipping out cross-correlates as shown. In this work, we reference the measurement to measurements with $H(\omega) = 1$ (nominally), simply by displacing the sample to a measurement region with no plasmon antennas (i.e., with only the reflector).

Sample. As metasurface, we use gold nanorods fabricated on a flat glass substrate in square arrays of various pitches made by e-beam lithography. We use a multistack for lift-off, consisting of an e-beam resist (top layer, thin for resolution), a thin germanium layer, and a thicker bottom spacer layer that generates the undercut and thickness needed for lift off. The germanium serves as an etch mask for the spacer. The fabrication procedure is as follows: we spin-coat 100 nm PMMA 495-A8 on cleaned glass slides (base piranha) followed by evaporation of 20 nm germanium. We then spin-coat 50 nm of CSAR AR-P 6200:09 as e-beam resist. Exposure of the sample is done in a Voyager e-beam system (Raith, 50 keV). The nanorod size (100 by 50 nm) is chosen to obtain a resonance in our lasing tuning window. We fabricate four different pitches, from dilute to dense (pitch 550, 433, 350, and 200 nm), as limited by the desire to avoid grating diffractions. We write 100 × 100 μm sized fields in rows with a spacing of 150 μm between the fields. This is chosen to accommodate a staircase of controlled glass thickness to be evaporated over the field to ultimately create etalons. After exposure, we develop the resist in pentyl acetate for 60 s. Next, the germanium is plasma etched in a 1:5 O_2:SF_6 mixture for 60 s, and PMMA is isotropically etched in an O_2 plasma. Finally, we evaporate 40 nm gold and perform liftoff in 45 °C acetone.

To obtain etalons of controlled spacing we evaporate SiO_x using e-beam evaporation (Polyteknik Flextura M508 E). A linear shutter is used to realize a staircase of increasing thickness ranging from 60 to 540 nm in steps of 17 nm, with each step spaced by 500 μm. Irrespective of the exact alignment of the staircase relative to the fields, this ensures that we obtain all lattice-height combinations. As a final step, the sample is covered with 50 nm gold as back reflector (providing an r_m of −0.95).

Measurement Protocol. Our optical measurement protocol consists of a sample and reference measurement at every spacer thickness, d, and runs through the following steps. First, we focus our sample beam on a nanorod field, with the nanorods' long axis aligned with the polarization of the sample beam (90 deg with respect to the lab frame, i.e., horizontally polarized). The orientation of the Wollaston prism dictates where the focus of the reference beam is positioned. In this work, the reference focus is vertically offset from the sample beam by 500 μm. Our sample design ensures that it lands on the back mirror of the etalon, and at the same spacer thickness, d (see right inset in Figure 3a). To span the spectrum from 640 to 900 nm (exceeding the 12 nm spectrum of our pulses), we take data at a sequence of pulse central frequencies. Subsequently, we perform a sequence of reference measurements after vertically shifting the sample to have both beams focusing on the mirror. Repeating this sequence for each spacer separation leads to the complex reflection r versus d and ω.

AUTHOR INFORMATION

Corresponding Author

*E-mail: f.koenderink@amolf.nl.

ORCID

A. Femius Koenderink: 0000-0003-1617-5748

Notes

The authors declare no competing financial interest.

ACKNOWLEDGMENTS

This work is part of the research programme *Hybrid nanophotonic architectures for ultrafast quantum optics [NWO-Vici]* with project number 680.47.621, which is financed by the Dutch Research Council (NWO) and was performed at the research institute AMOLF. The authors are grateful to M. Kamp for help setting up the femtosecond interferometry and

DOI: 10.1021/acsphotonics.9b01019
ACS Photonics XXXX, XXX, XXX−XXX

to the Amsterdam Nanocenter staff for their unwavering support regarding nanofabrication.

REFERENCES

(1) Yu, N.; Capasso, F. Flat optics with designer metasurfaces. *Nat. Mater.* **2014**, *13*, 139−150.
(2) Salisbury, W. W. Absorbent body for electromagnetic waves. U.S. Patent No. US2,599,944, 1952.
(3) Fante, R. L.; McCormack, M. T. Reflection properties of the Salisbury screen. *IEEE Trans. Antennas Propag.* **1988**, *36*, 1443−1454.
(4) Watts, C. M.; Liu, X.; Padilla, W. J. Metamaterial Electromagnetic Wave Absorbers. *Adv. Mater.* **2012**, *24*, OP98−OP120.
(5) Liu, N.; Mesch, M.; Weiss, T.; Hentschel, M.; Giessen, H. Infrared Perfect Absorber and Its Application As Plasmonic Sensor. *Nano Lett.* **2010**, *10*, 2342−2348.
(6) Aydin, K.; Ferry, V. E.; Briggs, R. M.; Atwater, H. A. Broadband polarization-independent resonant light absorption using ultrathin plasmonic super absorbers. *Nat. Commun.* **2011**, *2*, 517.
(7) Jang, M. S.; Brar, V. W.; Sherrott, M. C.; Lopez, J. J.; Kim, L.; Kim, S.; Choi, M.; Atwater, H. A. Tunable large resonant absorption in a midinfrared graphene Salisbury screen. *Phys. Rev. B: Condens. Matter Mater. Phys.* **2014**, *90*, 165409.
(8) Ra'di, Y.; Simovski, C. R.; Tretyakov, S. A. Thin Perfect Absorbers for Electromagnetic Waves: Theory, Design, and Realizations. *Phys. Rev. Appl.* **2015**, *3*, 037001.
(9) Alaee, R.; Albooyeh, M.; Rockstuhl, C. Theory of metasurface based perfect absorbers. *J. Phys. D: Appl. Phys.* **2017**, *50*, 503002.
(10) Pirruccio, G.; Martín Moreno, L.; Lozano, G.; Gómez Rivas, J. Coherent and Broadband Enhanced Optical Absorption in Graphene. *ACS Nano* **2013**, *7*, 4810−4817.
(11) Kakenov, N.; Balci, O.; Takan, T.; Ozkan, V. A.; Altan, H.; Kocabas, C. Observation of Gate-Tunable Coherent Perfect Absorption of Terahertz Radiation in Graphene. *ACS Photonics* **2016**, *3*, 1531−1535.
(12) Henseleit, T.; Sudzius, M.; Fröb, H.; Leo, K. Coherent perfect absorption in wedged organic thin films: a method to determine optical properties. *Opt. Lett.* **2018**, *43*, 4013−4016.
(13) Sima, B.; Chen, K.; Luo, X.; Zhao, J.; Feng, Y. Combining Frequency-Selective Scattering and Specular Reflection Through Phase-Dispersion Tailoring of a Metasurface. *Phys. Rev. Appl.* **2018**, *10*, 064043.
(14) Ding, F.; Yang, Y.; Deshpande, R. A.; Bozhevolnyi, S. I. A review of gap-surface plasmon metasurfaces: fundamentals and applications. *Nanophotonics* **2018**, *7*, 1129−1156.
(15) Munk, B. A. *Frequency Selective Surfaces: Theory and Design*; John Wiley & Sons: New York, 2005.
(16) Chong, Y. D.; Ge, L.; Cao, H.; Stone, A. D. Coherent Perfect Absorbers: Time-Reversed Lasers. *Phys. Rev. Lett.* **2010**, *105*, 053901.
(17) Wan, W.; Chong, Y.; Ge, L.; Noh, H.; Stone, A. D.; Cao, H. Time-Reversed Lasing and Interferometric Control of Absorption. *Science* **2011**, *331*, 889−892.
(18) Nielsen, M. G.; Pors, A.; Albrektsen, O.; Bozhevolnyi, S. I. Efficient absorption of visible radiation by gap plasmon resonators. *Opt. Express* **2012**, *20*, 13311−13319.
(19) Pors, A.; Bozhevolnyi, S. I. Plasmonic metasurfaces for efficient phase control in reflection. *Opt. Express* **2013**, *21*, 27438−27451.
(20) Chen, H.-T. Interference theory of metamaterial perfect absorbers. *Opt. Express* **2012**, *20*, 7165−7172.
(21) Alaee, R.; Farhat, M.; Rockstuhl, C.; Lederer, F. A perfect absorber made of a graphene micro-ribbon metamaterial. *Opt. Express* **2012**, *20*, 28017−28024.
(22) Christ, A.; Zentgraf, T.; Tikhodeev, S. G.; Gippius, N. A.; Kuhl, J.; Giessen, H. Controlling the interaction between localized and delocalized surface plasmon modes: Experiment and numerical calculations. *Phys. Rev. B: Condens. Matter Mater. Phys.* **2006**, *74*, 155435.
(23) Wang, Q.; Plum, E.; Yang, Q.; Zhang, X.; Xu, Q.; Xu, Y.; Han, J.; Zhang, W. Reflective chiral meta-holography: multiplexing holograms for circularly polarized waves. *Light: Sci. Appl.* **2018**, *7*, 25.
(24) Kumar, K.; Duan, H.; Hegde, R. S.; Koh, S. C. W.; Wei, J. N.; Yang, J. K. W. Printing colour at the optical diffraction limit. *Nat. Nanotechnol.* **2012**, *7*, 557−561.
(25) Miyata, M.; Hatada, H.; Takahara, J. Full-Color Subwavelength Printing with Gap-Plasmonic Optical Antennas. *Nano Lett.* **2016**, *16*, 3166−3172.
(26) Qu, C.; Ma, S.; Hao, J.; Qiu, M.; Li, X.; Xiao, S.; Miao, Z.; Dai, N.; He, Q.; Sun, S.; Zhou, L. Tailor the Functionalities of Metasurfaces Based on a Complete Phase Diagram. *Phys. Rev. Lett.* **2015**, *115*, 235503.
(27) Bowen, P. T.; Baron, A.; Smith, D. R. Theory of patch-antenna metamaterial perfect absorbers. *Phys. Rev. A: At., Mol., Opt. Phys.* **2016**, *93*, 063849.
(28) Solli, D. R.; McCormick, C. F.; Chiao, R. Y.; Popescu, S.; Hickmann, J. M. Fast Light, Slow Light, and Phase Singularities: A Connection to Generalized Weak Values. *Phys. Rev. Lett.* **2004**, *92*, 043601.
(29) Asano, M.; Bliokh, K. Y.; Bliokh, Y. P.; Kofman, A. G.; Ikuta, R.; Yamamoto, T.; Kivshar, Y. S.; Yang, L.; Imoto, N.; Ozdemir, S. K.; Nori, F. Anomalous time delays and quantum weak measurements in optical micro-resonators. *Nat. Commun.* **2016**, *7*, 13488.
(30) Kwadrin, A.; Osorio, C. I.; Koenderink, A. F. Backaction in metasurface etalons. *Phys. Rev. B: Condens. Matter Mater. Phys.* **2016**, *93*, 104301.
(31) Menzel, C.; Sperrhake, J.; Pertsch, T. Efficient treatment of stacked metasurfaces for optimizing and enhancing the range of accessible optical functionalities. *Phys. Rev. A: At., Mol., Opt. Phys.* **2016**, *93*, 063832.
(32) García de Abajo, F. J. Colloquium: Light scattering by particle and hole arrays. *Rev. Mod. Phys.* **2007**, *79*, 1267−1290.
(33) Thongrattanasiri, S.; Koppens, F. H. L.; García de Abajo, F. J. Complete Optical Absorption in Periodically Patterned Graphene. *Phys. Rev. Lett.* **2012**, *108*, 047401.
(34) Lunnemann, P.; Sersic, I.; Koenderink, A. F. Optical properties of two-dimensional magnetoelectric point scattering lattices. *Phys. Rev. B: Condens. Matter Mater. Phys.* **2013**, *88*, 245109.
(35) Sersic, I.; Tuambilangana, C.; Kampfrath, T.; Koenderink, A. F. Magnetoelectric point scattering theory for metamaterial scatterers. *Phys. Rev. B: Condens. Matter Mater. Phys.* **2011**, *83*, 245102.
(36) Kop, R. H. J.; Sprik, R. Phase-sensitive interferometry with ultrashort optical pulses. *Rev. Sci. Instrum.* **1995**, *66*, 5459−5463.
(37) Silva, A.; Monticone, F.; Castaldi, G.; Galdi, V.; Alù, A.; Engheta, N. Performing Mathematical Operations with Metamaterials. *Science* **2014**, *343*, 160−163.
(38) Wang, W.; Ramezani, M.; Vakevainen, A. I.; Torma, P.; Rivas, J. G.; Odom, T. W. The rich photonic world of plasmonic nanoparticle arrays. *Mater. Today* **2018**, *21*, 303−314.
(39) Svedendahl, M.; Verre, R.; Kall, M. Refractometric biosensing based on optical phase flips in sparse and short-range-ordered nanoplasmonic layers. *Light: Sci. Appl.* **2014**, *3*, e220.
(40) Kravets, V. G.; Schedin, F.; Jalil, R.; Britnell, L.; Gorbachev, R. V.; Ansell, D.; Thackray, B.; Novoselov, K. S.; Geim, A. K.; Kabashin, A. V.; Grigorenko, A. N. Singular phase nano-optics in plasmonic metamaterials for label-free single-molecule detection. *Nat. Mater.* **2013**, *12*, 304−309.
(41) Huang, F.; Drakeley, S.; Millyard, M. G.; Murphy, A.; White, R.; Spigone, E.; Kivioja, J.; Baumberg, J. J. Zero-Reflectance Metafilms for Optimal Plasmonic Sensing. *Adv. Opt. Mater.* **2016**, *4*, 328−335.
(42) Yan, C.; Raziman, T. V.; Martin, O. J. F. Phase Bifurcation and Zero Reflection in Planar Plasmonic Metasurfaces. *ACS Photonics* **2017**, *4*, 852−860.
(43) Sreekanth, K. V.; Sreejith, S.; Han, S.; Mishra, A.; Chen, X.; Sun, H.; Lim, C. T.; Singh, R. Biosensing with the singular phase of an ultrathin metal-dielectric nanophotonic cavity. *Nat. Commun.* **2018**, *9*, 369.
(44) van Dijk, M. A.; Lippitz, M.; Stolwijk, D.; Orrit, M. A common-path interferometer for time-resolved and shot-noise-limited detection of single nanoparticles. *Opt. Express* **2007**, *15*, 2273−2287.

DOI: 10.1021/acsphotonics.9b01019
ACS Photonics XXXX, XXX, XXX−XXX